

Research Article

Mesoporous Nickel-Based Zeolite Capsule Complex with Fe_3O_4 as Electrode for Advanced Supercapacitor

Lili Song,¹ Yinghui Han ,^{1,2,3} Feng Guo,⁴ Yunpeng Jiao,^{1,2} Yujuan Li,¹ Yunpeng Liu ,³ and Feng Gao²

¹Department of Mathematics & Physics, North China Electric Power University, Baoding, Hebei 071003, China

²Energy Internet Research, Tsinghua University, Beijing 100084, China

³Hebei Key Laboratory of Distributed Energy Storage and Micro-grid, North China Electric Power University, Baoding, Hebei 071003, China

⁴Department of Chemical Engineering, University of Wyoming, Laramie 82072, USA

Correspondence should be addressed to Yinghui Han; yinghuihan@ncepu.edu.cn and Yunpeng Liu; gylyp@263.net

Received 30 June 2018; Revised 20 September 2018; Accepted 27 September 2018; Published 19 December 2018

Guest Editor: Zhengping Zhou

Copyright © 2018 Lili Song et al. This is an open access article distributed under the Creative Commons Attribution License, which permits unrestricted use, distribution, and reproduction in any medium, provided the original work is properly cited.

A new kind of zeolite capsule complex with ferriferrous oxide (Fe_3O_4) materials was prepared in this work. Its morphology was characterized via the scanning electron microscope (SEM), the high-resolution transmission electron microscopy (HRTEM), N_2 adsorption analysis, and X-ray powder diffraction, respectively. The mesoporous nickel-based complex electrodes using substrate coating exhibited excellent energy storage properties through electrochemical testing. The high specific capacitance of 739.8 F g^{-1} was achieved at the current density of 1 A g^{-1} in a 6M KOH solution. The good capacitance retention can retain 72.8% after 1000 cycles in a current density of 1 A g^{-1} . The energy storage mechanism of the nickel-based complex electrodes was also analyzed. Furthermore, the asymmetrical supercapacitors (ASCs) were fabricated using the zeolite capsule complex with Fe_3O_4 as positive electrodes and the AC as negative electrodes, which performs high specific capacitance, outstanding energy density, superb power density, excellent cycle life, and small internal impedance. Those results suggest that the mesoporous nickel-based zeolite capsule complex with Fe_3O_4 as an electrode would be an ideal candidate material for supercapacitor applications.

1. Introduction

In recent years, the ecological environment has been deteriorating day by day. The development of new energy and renewable energy has aroused widespread concern. However, new energy and renewable energy have some disadvantages, such as instability and indirectness. Therefore, developing energy storage technology is an important guarantee for the popularization and application of new energy and renewable energy. As a power storage technology, supercapacitors have attracted much attention in terms of its high power density, fast charge and discharge rate, and long cycle life [1–5]. According to different energy storage mechanisms, the supercapacitors can be divided into double-layer capacitors (EDLCs) and pseudocapacitors [6, 7]. The supercapacitors

consist of three parts, i.e., the electrolyte, the electrode, and the diaphragm. The electrode and the electrolyte play the core role in improving the performance of the supercapacitors. The development of the electrode material has become one of the main research directions, and the trend of electrode materials has two main aspects of nanoscale and composite at present.

Mesoporous materials have become one of the research hotspots in the world because of their large specific surface area, regular pore structure, and excellent controllability. The research on mesoporous materials as electrodes is widely paid attention. Saravanakumar et al. [8] prepared vanadium pentoxide (V_2O_5)/nitrogen-containing mesoporous carbon spheres (n-MPC) nanocomposite without the use of expensive organic vanadium precursors and

sophisticated instruments. The optimal specific capacity was 410 Fg^{-1} . Lv et al. [9] developed the NiO/graphene composites. The electrochemical results showed that the NiO/graphene composites exhibited very high specific capacitance 1062 Fg^{-1} at 1 Ag^{-1} . The mesoporous structure of Ni(OH)₂ and NiO was synthesized using twelve alkyl sodium sulfate as a template, and its specific capacitance was about 106 Fg^{-1} [10]. However, among the reported materials, either the cost is too high or the performance is not good enough to meet the needs of the large-scale industrial application. In addition, it is still a challenge to design an electrode material allied with both high specific capacitance and excellent cycle life.

In this work, a new kind of cost-effective complex materials would be prepared via internal template method and suspension polymerization. The structure and morphology will be characterized using SEM, HRTEM, BET, and XRD. Finally, the electrochemical performance test of the asymmetrical supercapacitors (ASCs) in a three-electrode system will be performed by an electrochemical workstation. Those results aim at providing a reference and basic data for the preparation of industrial supercapacitor.

2. Experiment

2.1. Materials and Reagents. All starting chemicals were commercially available reagents with analytical grade and used without further purification, and all solutions were prepared with distilled water. Nickel foam (Tianjin Beichen Reagent Co. Ltd., China) was rinsed four times with distilled water and ethanol, respectively. Beer yeast was from Bozhou Baohua Pharmaceutical Co. Ltd., China. All the other reagents were from Baoding Huaxin Reagent Co. Ltd., China.

2.2. Preparation of Zeolite Template and the Nickel-Based Complex Electrode. In order to obtain the electrode with high performance for advanced supercapacitor, the zeolite template, the complex materials, and the nickel-based complex electrode were prepared, respectively.

Firstly, the beer yeast, as an auxiliary template, was immersed in hydrochloric acid by ultrasonic cleaning. The pretreatment went through repeated filtration, washing, and drying.

Secondly, the amount of sodium hydroxide was added into deionized water. After the dissolution, dropwise add a certain amount of sodium aluminate (NaAlO₂). The directing agent was prepared by maintaining at the reaction temperature (25°C) and stirring for 24 h.

Thus, a certain amount of auxiliary template was dissolved into distilled water and then a certain volume of directing agent was added. After mixing evenly, hydrochloric acid was dropwise to adjust the pH value of the reaction system until white floc appeared. Further, the mixed solution was transferred to a Teflon-lined heated reactor, reacted at 80°C for 5 hours, then suction filtered and dried at 50°C overnight. After grinding in a muffle furnace calcined at 150°C for 2 hours, the temperature was raised to 550°C calcined for 4 hours. In this case, the zeolite template was obtained.

A given amount of Fe₃O₄ ultrasonic mixing dissolved in a certain water. Subsequently, the zeolite template, a certain amount of iron ions, pyrimidine, and hydrogen peroxide solution were added into the solution successively. The mixture was stirred for 12 hours. Finally, the material of the zeolite capsule complex with Fe₃O₄ was synthesized after filtration, washing, and drying.

To prepare the electrodes for electrochemical measurements, the active materials, including the pure Fe₃O₄ and the zeolite capsule complex with Fe₃O₄, polytetrafluoroethylene (PTFE), and acetylene black were mixed with a mass ratio of 80:10:10 in anhydrous ethanol to form a homogeneous slurry. The working electrode was made by coating the viscous slurry onto nickel foam and then dried at 120°C to evaporate the solvent. After this process, the foam nickel loaded with the complex materials was directly sliced and pressed into circular electrodes of supercapacitors.

2.3. Characterizations. The morphologies were observed using a scanning electron microscope (SEM) equipped with a rapid energy dispersive X-ray spectrometer (EDS) research on a FEI Nova NanoSEM 450 microscope. The high-resolution transmission electron microscopy (HRTEM) images were analyzed through a HRTEM (JEOLJEM2100). The specific surface area was calculated using the Brunauer-Emmett-Teller (BET) model based on the N₂ adsorption branch within the relative pressure range of 0.05–0.35, and the pore size distribution was obtained from the N₂ desorption branch by the Barrett-Joyner-Halenda (BJH) method. The phase purity and crystallinity of the products were analyzed by X-ray powder diffraction (XRD, Rigaku, Japan) which were recorded on a RINT 2500 V X-ray diffractometer with Cu Kα radiation ($\lambda = 1.5406 \text{ \AA}$) at a scan rate $6^\circ/\text{min}$ in the 2θ range from 10° to 80° .

2.4. Electrochemical Measurement. The measurements of cyclic voltammetry (CV) and galvanostatic charge-discharge (GCD) were carried out in a 6 M KOH solution by electrochemical workstation (Chenhua CHI760E, Shanghai). Electrochemical impedance spectroscopy (EIS) was introduced to estimate the pseudocapacitor performance. An AC voltage with 5 mV amplitude in a range of 0.01 Hz– 10^5 Hz was used to estimate internal resistance of the electrode.

In order to achieve a comparison of the performance of different electrode materials, the specific capacitance was calculated, and the energy density and power density were estimated, respectively. For the CV curve, the charge of the electric potential between φ_1 and φ_2 can be obtained by integrating the volt-ampere curve with the rate $s = d\varphi/dt$ scanning:

$$Q = \int_{\varphi_1}^{\varphi_2} i(\varphi) dt \equiv \int_{\varphi_1}^{\varphi_2} \frac{i(\varphi) d\varphi}{s}, \quad (1)$$

where φ (V) is the electric potential, s (V s^{-1}) is the scanning rate, and t (s) is the scanning time [11].

Therefore, the specific capacitance is calculated according to the following equation [12, 13]:

$$C = \frac{Q}{2\Delta V \times m}, \quad (2)$$

where Q is the charge integrated from the whole voltage range, ΔV (V) is the whole voltage difference, and m (g) is the mass of active material in a single electrode.

In addition, the galvanostatic charge-discharge-specific capacities were calculated from the following equations [14–16]:

$$C = \frac{2i_m \int v dt}{(v_f - v_i)^2}, \quad (3)$$

where C (F g^{-1}) is specific capacitance, i_m (A g^{-1}) is applied discharge current density, $\int v dt$ is the integral current area of the galvanostatic charge-discharge curve, and v_f and v_i (V) are the potential with initial and final values, respectively.

Measurements of electrochemical performance of mesoporous complex materials and active carbon (AC) asymmetric supercapacitors were carried out via electrochemical workstation using 6 M KOH as the electrolyte. The preparation of the negative electrode directly applied activated carbon, acetylene black, and PTFE (80 wt%, 10 wt%, and 10 wt%) mixture onto the foam nickel, which was similar to the synthesis of nickel-based complex electrode.

In terms of the charge balance of asymmetric supercapacitors (ASCs), the principle $q^+ = q^-$ should be satisfied, where q^+ is the positive charges and q^- is the negative charges. The voltammetric charges (q) were obtained by the following equation [17, 18]:

$$q = C \times \Delta V \times m, \quad (4)$$

where C is the specific capacitance (F g^{-1}) of each electrode, ΔV is the potential windows (V), and m is the mass loading (g). So the mass ratio of the positive and negative electrode followed equation as [19]:

$$\frac{m_+}{m_-} = \frac{C_- \times \Delta V_-}{C_+ \times \Delta V_+}. \quad (5)$$

The energy density and power density of the ACSs were calculated by the following equations, respectively:

$$E = \frac{1}{2 \times 3.6} C (\Delta V)^2, \quad (6)$$

$$P = \frac{E \times 3600}{\Delta t}, \quad (7)$$

where E is the specific energy (Wh kg^{-1}), C is specific capacitance (F g^{-1}), Δt is discharge time (s), P is the specific power

(W kg^{-1}), and ΔV (V) is operating potential window of the ASCs [18, 20].

3. Results and Discussion

3.1. Structural and Morphological Study. Generally, the preparation process and growth conditions will directly affect the morphology and microstructure of complex materials. As the above section mentioned, the whole process of preparation is illustrated in Figure 1.

The morphology and structures of pure Fe_3O_4 , zeolite template, the complex material, and the nickel-based complex electrode on nickel foam are characterized in Figure 2, respectively. The pure Fe_3O_4 exhibits an excellent bulk structure and single crystal form, as shown in Figures 2(a) and 2(b), respectively. The structures of zeolite template show the great sheet-like pore structure (Figures 2(c)–2(e)). The EDS analysis (Figure 2(k)) of the zeolite template, revealing the presence of C, O, Al, Si, and Cl, and the atomic ratio of C to O, is approximately estimated to be 19.33:58.92. Comparing the SEM of the zeolite template (Figures 2(c)–2(e)) with that of the complex material (Figures 2(f)–2(h)), the complex material exhibits smaller particles and more porous structure for better storage of electrolyte ions and reducing the ion diffusion distance [21]. Furthermore, the EDS (Figure 2(l)) spectra of the complex materials showed the presence of C, N, O, and Fe, and the atomic ratio of C, N, and O to Fe is approximately estimated to be 11.86:3.04:41.56:43.55. The SEM images of the nickel-based complex electrodes (Figures 2(i) and 2(j)) with the magnification $40 \mu\text{m}$ and 500 nm , respectively, showed that the complex material is well attached to the nickel film. Meanwhile, the uniform hole distribution and structures were observed; that is probably one of the reasons why it has the excellent electrochemical performance for the supercapacitor electrode.

Furthermore, the HRTEM images of the nickel-based complex electrode at different magnifications in the range of 5 nm – 200 nm are depicted in Figure 3. The dark area in Figures 3(a) and 3(b) were supposed to be the aggregates of Fe_3O_4 and zeolite template agent in the dry state. The transparent short rods in Figure 3(c) showed the capsuling-like structure of the sample [22]. In addition, a clearly visible nanostave microstructure was observed in Figure 3(d), which would significantly reduce the ion diffusion distance and improve the charge transfer [23, 24].

Because surface and pore-size distribution are two key parameters for electroactive materials in energy conversion/storage applications [25], the N_2 adsorption analyses were carried out. From Figure 4, it is clearly seen that the complex materials have typical IV isotherms with H_3 -type hysteresis loop in the relative pressure (P/P_0) range of 0.6–1.0, indicating the presence of a mesoporous structure, while the zeolite template exhibits typical II isotherms that is characteristic for nonporous/macro porous materials. Furthermore, the pore-size distribution (inset of Figure 3) of the complex materials possesses mesoporous with a relative narrow size distribution in the range from 2 nm to

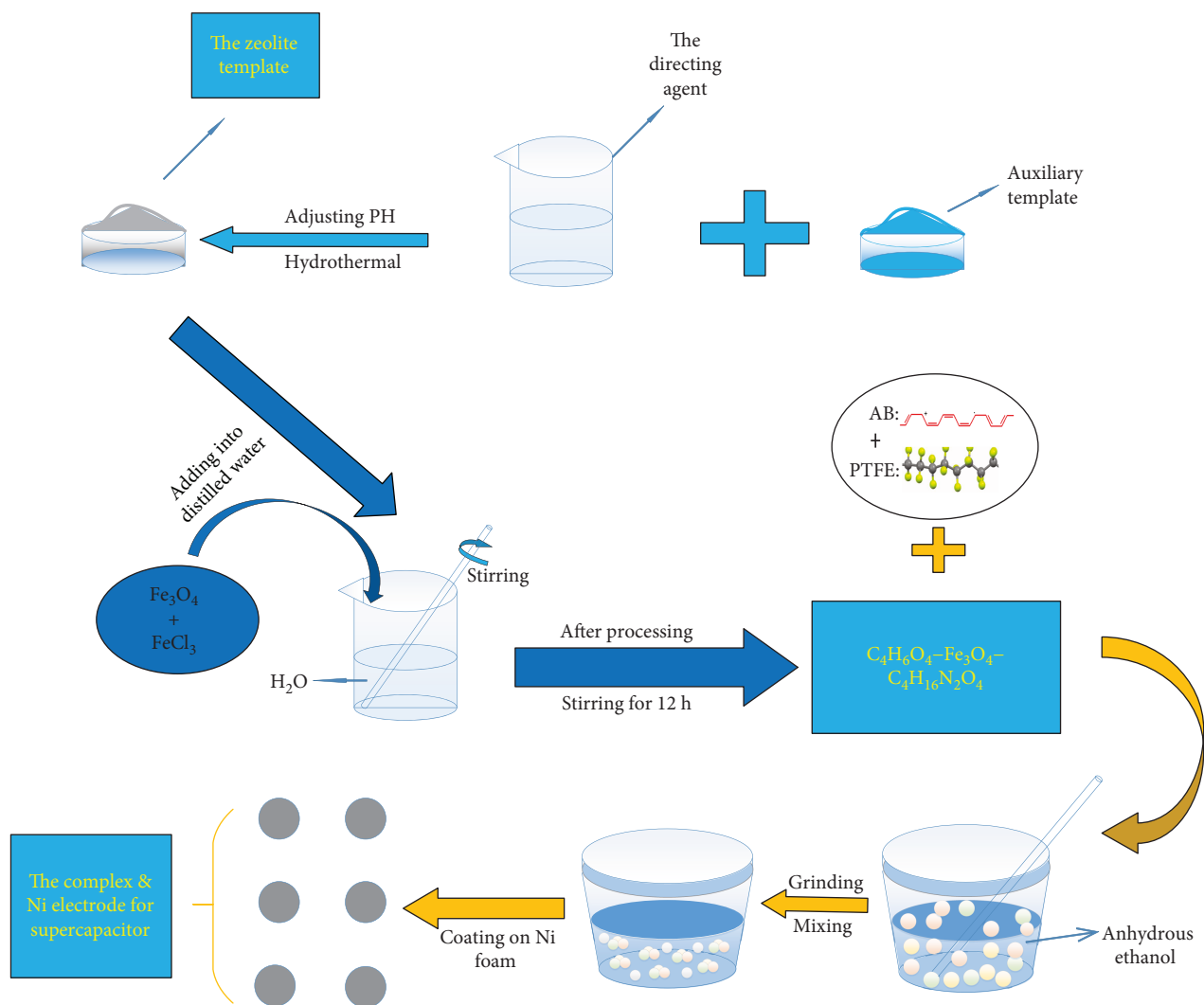


FIGURE 1: The schematic diagram of nickel-based supercapacitor electrode via the zeolite capsule complex with Fe_3O_4 .

10 nm by Barrett-Joyner-Halenda (BJH) method. Compared with the zeolite template, the complex materials reveal a relatively good specific surface area ($13.437\text{m}^2\text{g}^{-1}$) and total pore volume ($0.052\text{cm}^3\text{g}^{-1}$) calculated via Brunauer-Emmett-Teller (BET). Relatively good specific surface area and pore structure should enhance the electrode reaction kinetics [26–28], leading to better electrochemical performance.

To further identify the crystal structure and phase composition of all the samples, X-ray diffraction (XRD) analyses were carried out. As shown in Figure 5, those are the X-ray diffraction patterns of the pure Fe_3O_4 , the zeolite template, and the complex materials, respectively. It is obtained that the diffraction peaks of the pure Fe_3O_4 are in good agreement with those in the PDF standard card (JCPDS card NO.19-0629), and any peaks for the other secondary phases were not observed. It demonstrates that the pure Fe_3O_4 crystallizes in a pure phase. According to the PDF standard cards NO.44-0704 and NO.43-1522, it can be clearly seen that the zeolite template and the complex materials are marked unnamed zeolite (the chemical formula

is $\text{C}_3\text{H}_6\text{O}_2\cdot 6\text{SiO}_2$) and magnetite-tartrate-quadrol complex (the chemical formula is $\text{C}_4\text{H}_6\text{O}_6\text{-Fe}_3\text{O}_4\text{-C}_{14}\text{H}_{16}\text{N}_2\text{O}_4$), respectively. The pure Fe_3O_4 , the zeolite template, and the composite materials occur most commonly in the crystal structure of cubic I-43m, cubic Fd-3m, and cubic I-43m, respectively. The good matching peaks indicate that the zeolite template and the complex materials belong to a crystal form.

The morphological specific surface area and crystal structure were detected by SEM, HRTEM, N_2 adsorption analyses, and XRD, respectively. It can be well prepared for further analysis of the energy storage mechanism of the sample.

3.2. Electrochemical Performance. In order to study the electrochemical energy storage performance of the nickel-based complex electrodes for supercapacitors, the CV, GCD, and EIS were measured, respectively, in a three-electrode cell (vs. SCE) by electrochemical workstation (Chenhua CHI760E, Shanghai).

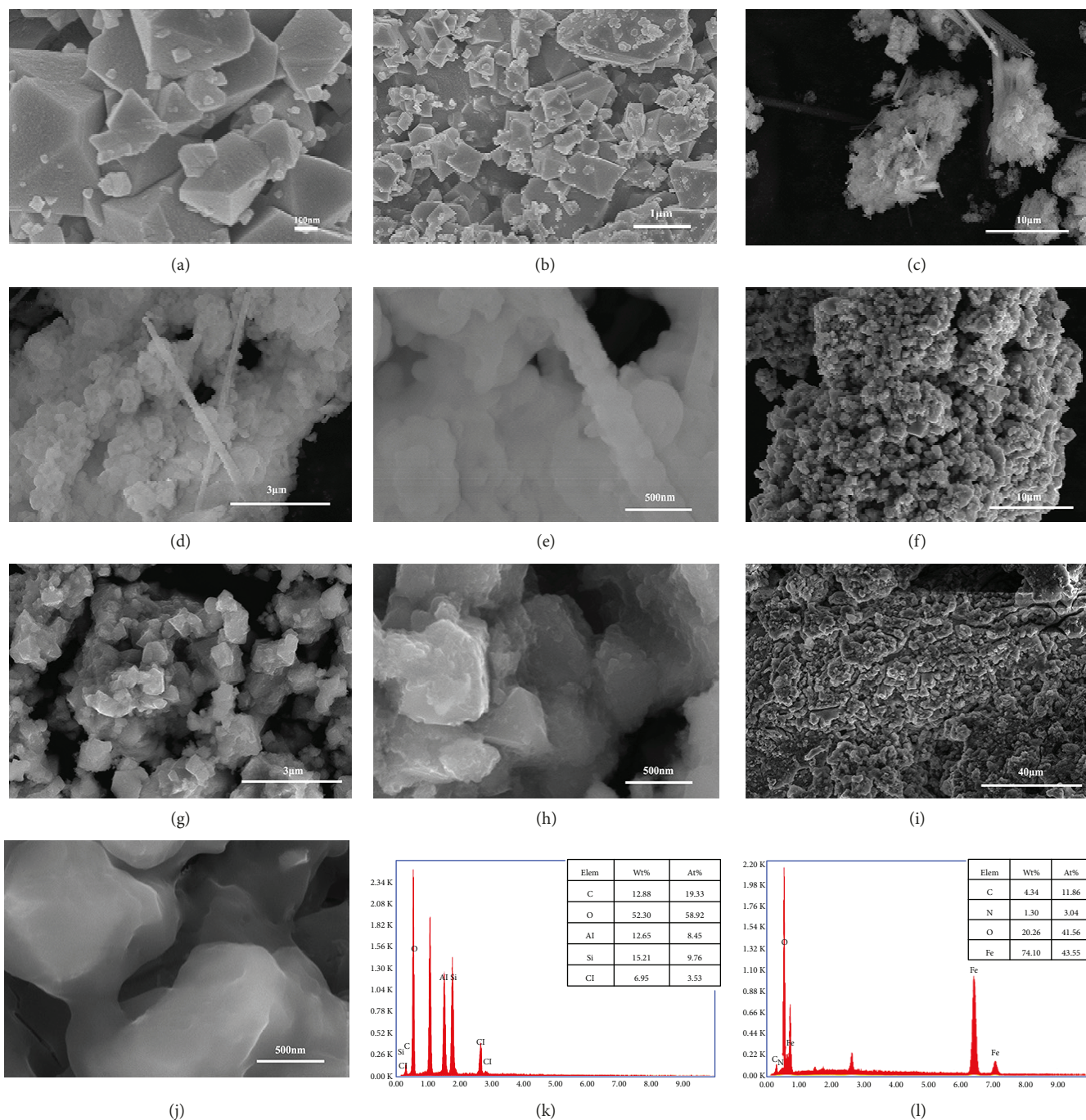


FIGURE 2: The SEM images at different magnification of the pure Fe_3O_4 (a–b), the zeolite template (c–e), the complex materials (f–h), and the nickel-based complex electrode (i–j), respectively. The EDS spectra of the zeolite template (k) and the complex materials (l).

Figure 6(a) shows the CV curve of the nickel-based complex electrodes and the pure nickel-based Fe_3O_4 electrodes at a scan rate of 10 mV s^{-1} . For the nickel-based complex electrodes of supercapacitors, one pair of redox peaks exhibited in CV curves in the range from -0.1 to 0.3 V , demonstrating that it stores energy through Faraday redox reaction. It has a pseudopotential characteristic, while the CV curve of the pure Fe_3O_4 electrodes is close to a smooth line. According to (1) and (2), the CV curve of the

nickel-based complex electrodes exhibits a larger integral area than that of the pure nickel-based Fe_3O_4 electrodes, indicating that the nickel-based complex electrode has a larger capacitance than that of the pure nickel-based Fe_3O_4 electrodes. To further contrast the electrochemical performance difference between the two electrodes, the GCD tests of both (Figure 6(b)) were conducted at current densities of 1 A g^{-1} . The longer discharge time of the nickel-based complex electrodes revealed that it has the higher

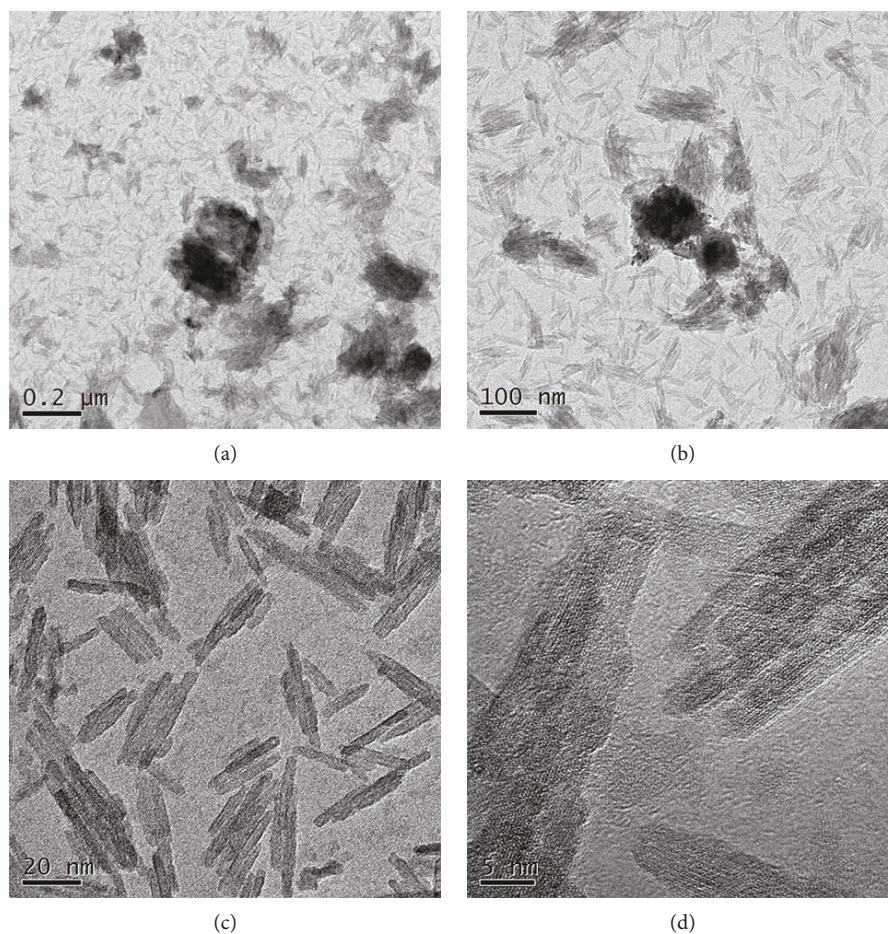


FIGURE 3: HRTEM images of the nickel-based complex electrode at different magnification.

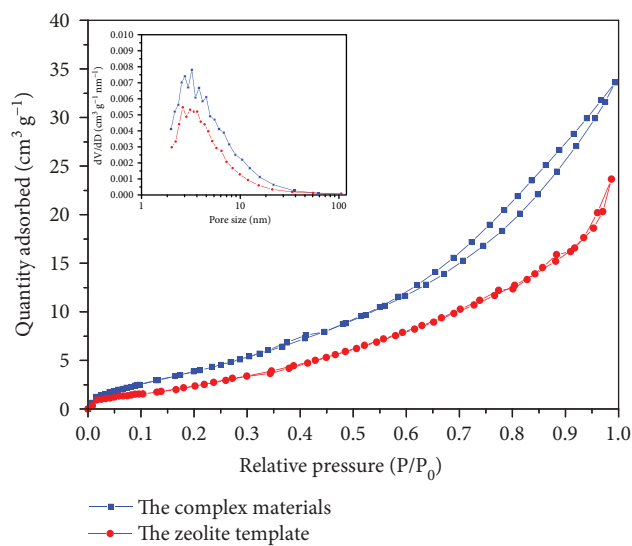


FIGURE 4: N_2 adsorption isotherms (inset: the curve of pore-size distribution).

electrochemical performance, which was similar to the CV results. Figures 6(c) and 6(d) showed the rate performance at different scanning rates and current densities. Along with

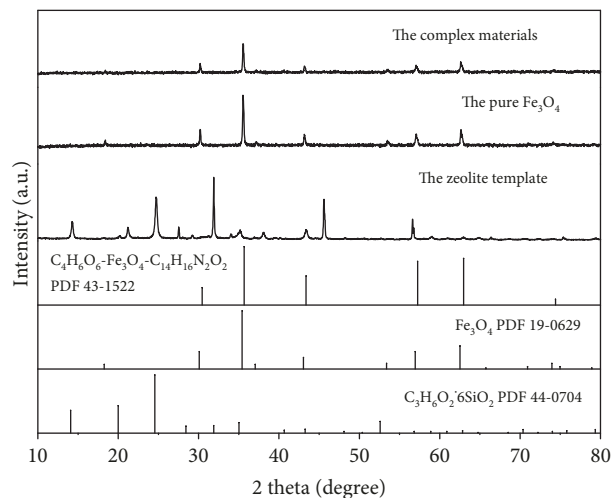


FIGURE 5: X-ray diffraction patterns of the pure Fe_3O_4 , the zeolite template, and the complex materials, respectively.

the increase of scanning rate, the position of the anodic peaks shifted to higher potential, in consistency with Randles-Sevcik rules [29]. With the increase of current density, the discharge time becomes shorter. The anodic

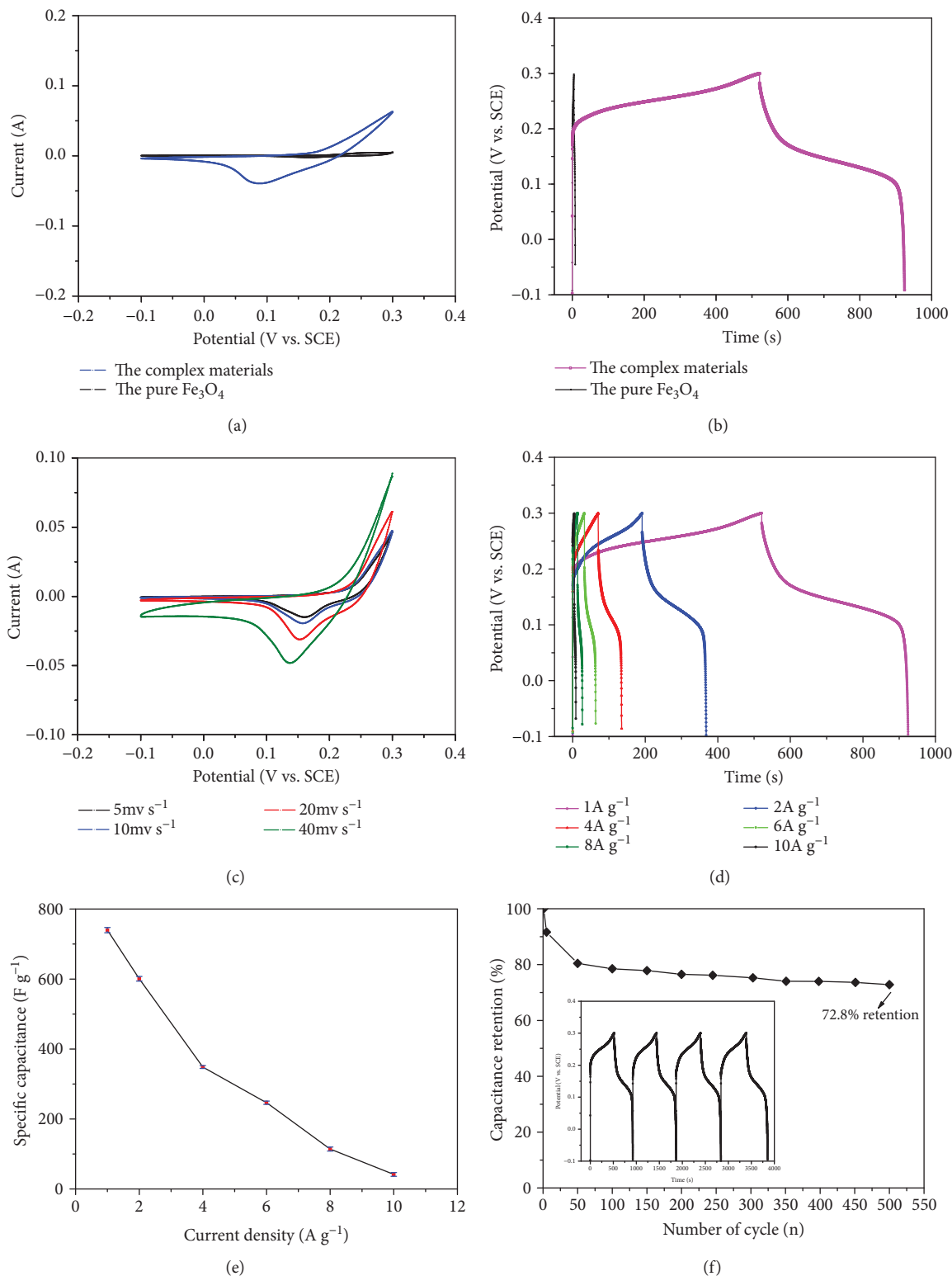


FIGURE 6: (a) CV curves of the nickel-based complex electrodes and the pure nickel-based Fe_3O_4 electrodes at a scan rate of 10 mV s^{-1} ; (b) GCD curves of the nickel-based complex electrodes and the pure nickel-based Fe_3O_4 electrodes at current densities of 1 A g^{-1} ; (c) CV curves of the nickel-based complex electrodes at different scanning rates; (d) GCD curves of the nickel-based complex electrodes at various current densities; (e) specific capacitance of the nickel-based complex electrode discharge curves at various current densities; and (f) cycling performance of the nickel-based complex electrodes measured at a voltage window of -0.1 V to 0.3 V .

peak shift probably results from polarization [30–32]. It clearly manifests that the nickel-based complex electrodes have excellent rate characteristics.

In order to observe the different current scanning rates of special capacitance changes, the specific capacitance of the nickel-based complex electrode at various current densities is calculated by (3) (Figure 6(e)). It is obvious that the specific capacitance decreases gradually with the increase of discharge current density. It can be seen that the specific capacitances of the nickel-based complex electrodes at the current density of 1, 2, 4, 6, 8, and 10 A g⁻¹ are 739.8, 600.8, 348.4, 246.5, 114, and 41.5 F g⁻¹, respectively. As the current density increases, the specific capacitance becomes smaller. This indicates both high specific capacitance and good capacitance retention at high rate.

Long-term cyclic stability is an important requirement for its applications in supercapacitors [33, 34]. As shown in Figure 6(f), the curve that the capacitance retention follows the number of the charge-discharge cycles is observed. And the inset is a partial GCD curve that was used to calculate the specific capacitance retention according to the following equations [35]:

$$\Delta C = |C_{\text{low}} - C_{\text{high}}|, \quad (8)$$

$$\alpha = \frac{\Delta C}{C_{\text{high}}} \times 100\%, \quad (9)$$

$$\beta = 1 - \alpha, \quad (10)$$

where C_{high} and C_{low} are the values of specific capacitance at -0.1 V and 0.3 V calculated by (3). β is the capacitance retention.

The capacitance retention reduced with the increase of the number of cycle because of consumption of active materials during energy storage. In the cycle number of 1 to 100, the capacity retention sharply drops due to the activation of the electrode material, while the capacity retention slows down after the cycle number of 100. The favorable capacitance retention retained 72.8% after 1000 cycles in a current density of 1 A g⁻¹. The good stability of the long-term cycle shows that it has considerable application prospects of electrodes for advance supercapacitor.

To evaluate the resistance of the nickel-based complex electrodes, an electrochemical impedance spectroscopy (EIS) was utilized. Figure 7 exhibits the Nyquist plots extracted from the EIS measurement on the nickel-based complex electrode in the frequency range of 0.01 Hz–10⁵ Hz. The inset image shows a Randles equivalent circuit and an enlarged picture of high-frequency curve, respectively. The impedance characteristics were simulated by ZsimpWin software. From the fitting data, it can be clearly obtained that the values of solution resistance (R_s) and charge-transfer resistance (R_{ct}) are 0.741 Ω and 0.0027 Ω , respectively, indicating a very low internal resistance charge-transfer resistance of the nickel-based complex electrode [36, 37].

3.3. Reaction Mechanism. From the electrochemical test results, the electrode is driven by a reversible Faraday

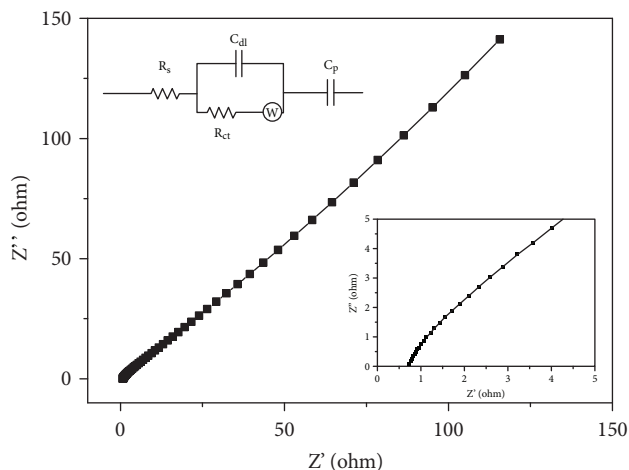


FIGURE 7: Complex plane impedance plots (Nyquist plots) of the nickel-based complex electrodes (inset: a Randles equivalent circuit, where R_s and R_{ct} are the solution and charge-transfer resistance, respectively. W , C_{dl} , and C_p are the Warburg resistance, electric double layer capacitance, and pseudocapacitive element; and an enlarged picture of high-frequency curve).

oxidation-reduction reaction. According to previous work [38–41], the mechanism might base on the following reactions:

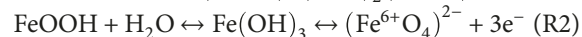
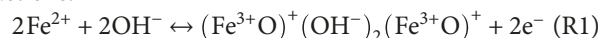


Figure 8 shows a conjecture diagram of the nickel-based complex electrode redox reaction. The nickel foam, as a good substrate material, is very suitable as the electrode of supercapacitors. In addition, the advantage of porous structure of the complex materials contains not only promoting electrolyte access and ion transport but also improving the contact opportunities between electrode material and electrolyte ion [42]. The synergy between the two materials might be one of the important reasons for the high electrochemical performance. The reasons mentioned above are the factors accounting for the high performance of the nickel-based complex electrode for the supercapacitor.

3.4. Performance Analysis of Asymmetrical Supercapacitors.

In order to obtain the complex materials in supercapacitor applications, the asymmetrical supercapacitors (ASCs) were fabricated using the zeolite capsule complex with Fe₃O₄ as positive electrodes and the AC as negative electrodes. Figure 9(a) shows the CV curve of the ASCs at different working cell potentials including 0 to 0.8, 0 to 1.0, 0 to 1.2, 0 to 1.4, and 0 to 1.5 V at 10 mV s⁻¹. Fortunately, there is an obvious H₂ or O₂ evolution switching potential indicating the excellent voltage range. As shown in Figure 9(b), this presents the CV curve of the cell at different scan rates from 5 to 100 mV s⁻¹ within a 0–1.5 V potential window. It can be clearly obtained that the energy storage was contributed via both capacitive (0–0.6 V) and faradaic (0.6–1.5 V) behavior. And it illustrates the good electrochemical reversibility and low internal resistance of the device [43]. The specific

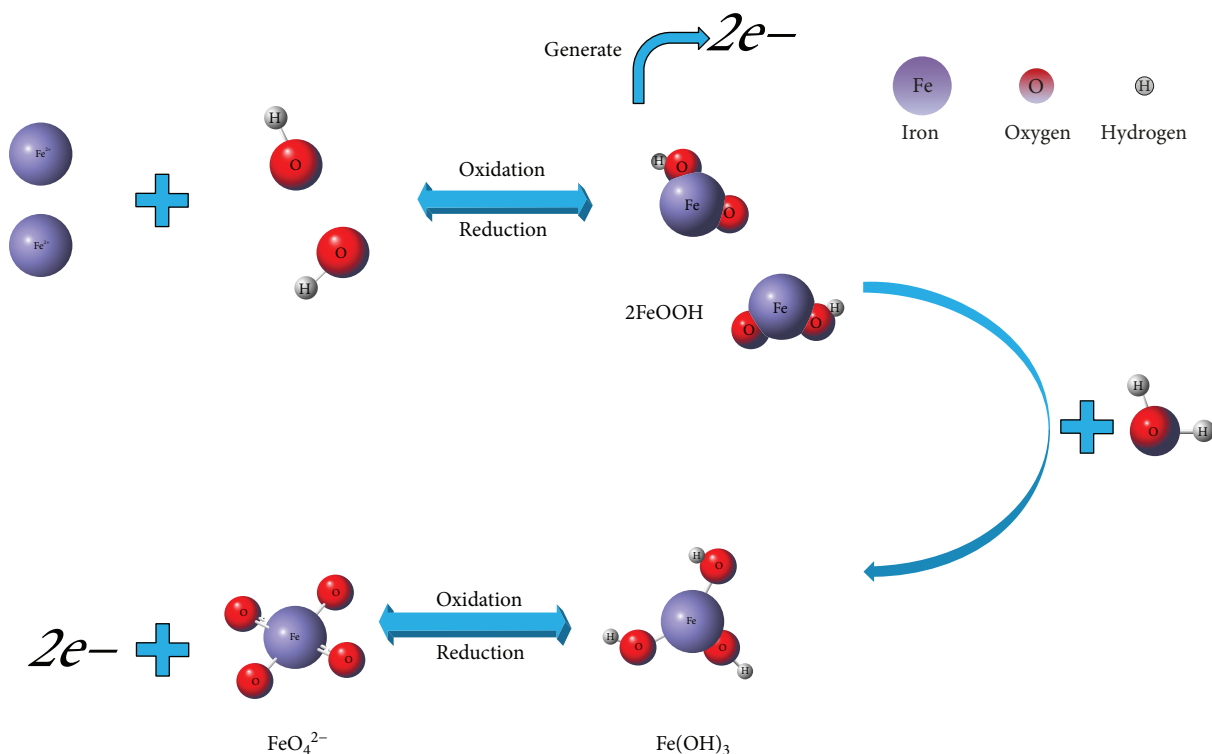


FIGURE 8: The conjecture mechanism of the Faraday oxidation-reduction reaction.

capacitance of the device was calculated using (1) and (2) at different scan rates in Figure 9(c). It can be seen that the ASCs exhibit a specific capacitance of about 105.9 F g^{-1} at 5 mV s^{-1} .

Figure 9(d) presents the GCD curve of the Ni-based complex//AC ASCs with cell voltage from 0 to 1.5 V at various current densities ($1\text{--}10 \text{ A g}^{-1}$). During the charge/discharge steps, the smaller IR or potential drop shows that the ASCs have less energy loss [44]. Unfortunately, the discharge time of the asymmetrical supercapacitor is slightly lesser than charge time. To observe the different current scanning rates of special capacitance changes, the mass specific capacitance of the nickel-based complex//AC ASCs at various current densities was calculated by (3) (Figure 9(e)). The specific capacitances of the ASCs at the current density of 1, 2, 3, 5, 8, and 10 A g^{-1} are 117.2, 97.1, 85.2, 69.5, 53.4, and 45.6 F g^{-1} , respectively. Further, the energy and power densities were calculated by (6) and (7), respectively. Figure 9(f) represents the variation of power density with energy density. The device transmits maximum energy density and power density of 36.6 Wh kg^{-1} and 916.1 W kg^{-1} , respectively.

Furthermore, the cyclic stability (Figure 10(a)) was carried up to 1000 cycles at current density of 1 A g^{-1} using 2 M KOH as the electrolyte. It is observed that the ASCs can keep 80.3% of initial capacitance over 1000 cycles, and the specific capacitance retention can remain stable after 550 cycles, which suggests that the ASCs display excellent stability. Finally, Figure 10(b) shows the impedance Nyquist plot of the ASC device from the fitted EIS data (the equivalent

circuit is the same as Figure 6). R_s and R_{ct} are 0.8046Ω and 0.05924Ω , respectively, indicating the low internal resistance and charge transfer resistance of the ASC device.

4. Conclusions

In this work, the mesoporous complex materials (the zeolite capsule complex with Fe_3O_4) with zeolite template capsule as the electrodes for supercapacitors were synthesized through suspension polymerization composite method and internal template method, respectively. The results showed that the high specific capacitance of the nickel-based complex electrode reaches as high as 739.8 F g^{-1} , and capacitance still retains 72.8% after 1000 cycles at current density of 1 A g^{-1} in 6 M KOH solution, indicating that the electrode materials have excellent electrochemical performances including high specific capacitance, excellent charge-discharge stability, good long-term cycling life, and small impedance. Moreover, the asymmetrical supercapacitors (ASCs) were fabricated using the zeolite capsule complex with Fe_3O_4 as positive electrodes and the AC as negative electrodes. It reveals high specific capacitance, outstanding energy density, and superb power density up to 117.2 F g^{-1} , 36.6 Wh kg^{-1} , and 916.1 W kg^{-1} at the current density of 1 A g^{-1} using 6 M KOH solution as electrolyte, respectively. Finally, the specific capacitance retains 80.3% after 1000 cycles at current density of 1 A g^{-1} in 2 M KOH solution, and the smaller internal impedance is obtained. It can be used as a promising electrode material for advanced supercapacitor.

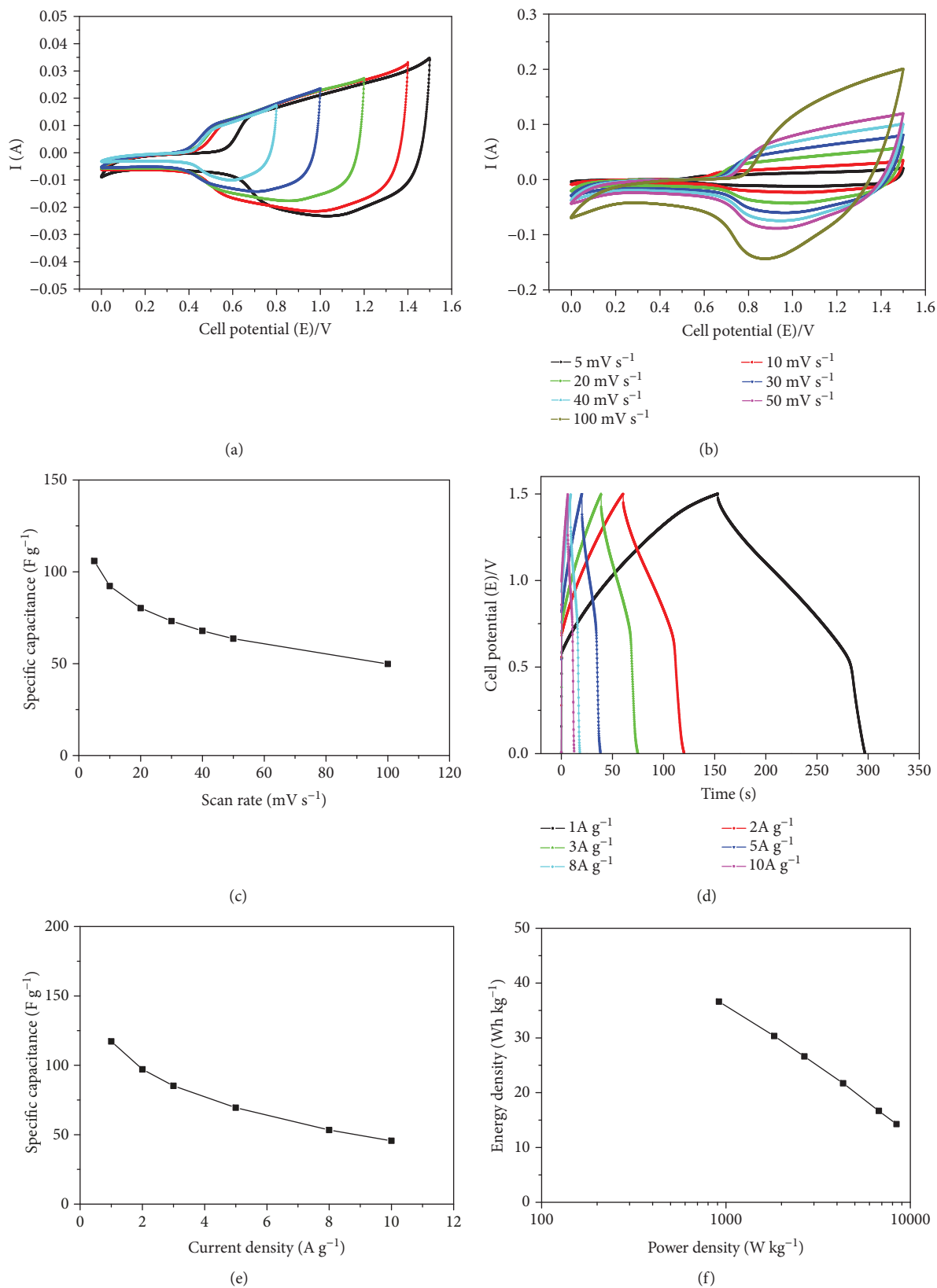


FIGURE 9: CV curve of the device (a) at different working potential window at 10 mV s^{-1} , (b) different scan rates, (c) variation of capacitance with scan rates, (d) GCD curves of the cell at various current densities, (e) specific capacitance at various current densities, and (f) Ragone plots of the energy and power densities of the device at various charge/discharge rates.

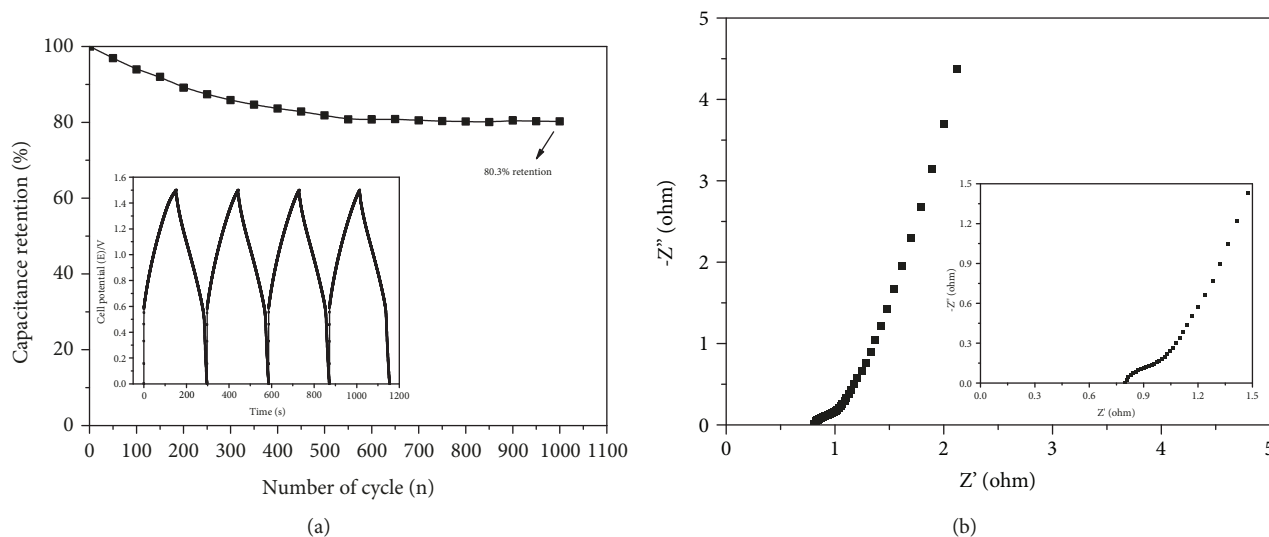


FIGURE 10: (a) The cycling performance of the device at 1 A g^{-1} for 1000 cycle and (b) Nyquist plots of the asymmetrical device.

Data Availability

The data used to support the findings of this study are available from the corresponding author upon request.

Conflicts of Interest

The authors declare no conflict of interest.

Authors' Contributions

LS was responsible for the original draft preparation and experimental implementation. YH was responsible for research ideas and scheme design. FG was responsible for review writing and grammar editing. YH and YL were responsible for the funding support. YJ and YL were responsible for characterization, and FG was responsible for the visualization. Lili Song and Yinghui Han contributed equally to this work.

Acknowledgments

This research was supported by the National Key R&D Plan (no. 2017YFC0210202-1), the Fundamental Research Funds for the Central Universities of China (no. 2015ZZD3), and the National Natural Science Foundation of China (no. 51308212).

References

- [1] N. Konikkara and L. J. Kennedy, "Electrochemical properties of solid leather wastes based supercapacitor electrodes using H_2SO_4 electrolyte," *Materials Letters*, vol. 205, pp. 56–61, 2017.
- [2] A. Eftekhari, "Supercapacitors utilising ionic liquids," *Energy Storage Materials*, vol. 9, pp. 47–69, 2017.
- [3] Y. Han, L. Li, Y. Liu, X. Li, X. Qi, and L. Song, "Fabrication of strontium bismuth oxides as novel battery-type electrode materials for high-performance supercapacitors," *Journal of Nanomaterials*, vol. 2018, Article ID 5078473, 10 pages, 2018.
- [4] P. Zhou, L. Fan, J. Wu, C. Gong, J. Zhang, and Y. Tu, "Facile hydrothermal synthesis of NiTe and its application as positive electrode material for asymmetric supercapacitor," *Journal of Alloys and Compounds*, vol. 685, pp. 384–390, 2016.
- [5] G.-S. Jang, S. Ameen, M. S. Akhtar, and H.-S. Shin, "Cobalt oxide nanocubes as electrode material for the performance evaluation of electrochemical supercapacitor," *Ceramics International*, vol. 44, no. 1, pp. 588–595, 2018.
- [6] Y.-P. Gao, K.-J. Huang, H.-L. Shuai, and L. Liu, "Synthesis of sphere-feature molybdenum selenide with enhanced electrochemical performance for supercapacitor," *Materials Letters*, vol. 209, pp. 319–322, 2017.
- [7] Z. Wang, C. Ma, H. Wang, Z. Liu, and Z. Hao, "Facilely synthesized Fe_2O_3 -graphene nanocomposite as novel electrode materials for supercapacitors with high performance," *Journal of Alloys and Compounds*, vol. 552, no. 1, pp. 486–491, 2013.
- [8] B. Saravanakumar, K. K. Purushothaman, and G. Muralidharan, " V_2O_5 / nitrogen enriched mesoporous carbon spheres nanocomposite as supercapacitor electrode," *Microporous and Mesoporous Materials*, vol. 258, pp. 83–94, 2018.
- [9] J. Lv, Z. Wang, and H. Miura, "Facile synthesis of mesoporous NiO nanoflakes on graphene foam and its electrochemical properties for supercapacitor application," *Solid State Communications*, vol. 269, pp. 45–49, 2018.
- [10] W. Xing, F. Li, Z. Yan, and G. Q. Lu, "Synthesis and electrochemical properties of mesoporous nickel oxide," *Journal of Power Sources*, vol. 134, no. 2, pp. 324–330, 2004.
- [11] M.-J. Deng, J.-K. Chang, C.-C. Wang et al., "High-performance electrochemical pseudo-capacitor based on MnO_2 nanowires/Ni foam as electrode with a novel Li-ion quasi-ionic liquid as electrolyte," *Energy & Environmental Science*, vol. 4, no. 10, pp. 3942–3946, 2011.
- [12] L. Jiang, J. Yan, L. Hao, R. Xue, G. Sun, and B. Yi, "High rate performance activated carbons prepared from ginkgo shells for electrochemical supercapacitors," *Carbon*, vol. 56, no. 56, pp. 146–154, 2013.

- [13] H.-L. Jiang, B. Liu, Y.-Q. Lan et al., "From metal-organic framework to nanoporous carbon: toward a very high surface area and hydrogen uptake," *Journal of the American Chemical Society*, vol. 133, no. 31, pp. 11854–11857, 2011.
- [14] H. Li, L. McRae, C. J. Firby, M. al-Hussein, and A. Y. Elezzabi, "Nanohybridization of molybdenum oxide with tungsten molybdenum oxide nanowires for solution-processed fully reversible switching of energy storing smart windows," *Nano Energy*, vol. 47, pp. 130–139, 2018.
- [15] L.-Q. Mai, A. Minhas-Khan, X. Tian et al., "Synergistic interaction between redox-active electrolyte and binder-free functionalized carbon for ultrahigh supercapacitor performance," *Nature Communications*, vol. 4, no. 1, 2013.
- [16] X. Xiong, D. Ding, D. Chen et al., "Three-dimensional ultrathin Ni(OH)₂ nanosheets grown on nickel foam for high-performance supercapacitors," *Nano Energy*, vol. 11, pp. 154–161, 2015.
- [17] K. N. Hui, K. S. Hui, Z. Tang, V. V. Jadhav, and Q. X. Xia, "Hierarchical chestnut-like MnCo₂O₄ nanoneedles grown on nickel foam as binder-free electrode for high energy density asymmetric supercapacitors," *Journal of Power Sources*, vol. 330, pp. 195–203, 2016.
- [18] X. Qi, W. Zheng, G. He, T. Tian, N. Du, and L. Wang, "NiCo₂O₄ hollow microspheres with tunable numbers and thickness of shell for supercapacitors," *Chemical Engineering Journal*, vol. 309, pp. 426–434, 2017.
- [19] K. Vijaya Sankar and R. Kalai Selvan, "Fabrication of flexible fiber supercapacitor using covalently grafted CoFe₂O₄/reduced graphene oxide/polyaniline and its electrochemical performances," *Electrochimica Acta*, vol. 213, pp. 469–481, 2016.
- [20] C.-S. Dai, P.-Y. Chien, J.-Y. Lin et al., "Hierarchically structured Ni₃S₂/carbon nanotube composites as high performance cathode materials for asymmetric supercapacitors," *ACS Applied Materials & Interfaces*, vol. 5, no. 22, pp. 12168–12174, 2013.
- [21] D. Xiang, L. Yin, C. Wang, and L. Zhang, "High electrochemical performance of RuO₂-Fe₂O₃ nanoparticles embedded ordered mesoporous carbon as a supercapacitor electrode material," *Energy*, vol. 106, pp. 103–111, 2016.
- [22] W. Yang, Z. Gao, N. Song, Y. Zhang, Y. Yang, and J. Wang, "Synthesis of hollow polyaniline nano-capsules and their supercapacitor application," *Journal of Power Sources*, vol. 272, pp. 915–921, 2014.
- [23] Y. Obukuro, S. Matsushima, K. Obata et al., "Effects of La doping on structural, optical, electronic properties of Sr₂Bi₂O₅ photocatalyst," *Journal of Alloys and Compounds*, vol. 658, pp. 139–146, 2016.
- [24] Y. C. Zhang, H. Yang, W. P. Wang et al., "A promising supercapacitor electrode material of CuBi₂O₄ hierarchical microspheres synthesized via a coprecipitation route," *Journal of Alloys and Compounds*, vol. 684, pp. 707–713, 2016.
- [25] X. Li, J. Zhou, X. Li et al., "Bifunctional petaloid nickel manganese layered double hydroxides decorated on a freestanding carbon foam for flexible asymmetric supercapacitor and oxygen evolution," *Electrochimica Acta*, vol. 252, pp. 275–285, 2017.
- [26] J. Zhao, J. Chen, S. Xu et al., "Hierarchical NiMn layered double hydroxide/carbon nanotubes architecture with superb energy density for flexible supercapacitors," *Advanced Functional Materials*, vol. 24, no. 20, pp. 2938–2946, 2014.
- [27] W. Lu, R. Hartman, L. Qu, and L. Dai, "Nanocomposite electrodes for high-performance supercapacitors," *Journal of Physical Chemistry Letters*, vol. 2, no. 6, pp. 655–660, 2011.
- [28] M. Liu, J. Li, W. Han, and L. Kang, "Simple synthesis of novel phosphate electrode materials with unique microstructure and enhanced supercapacitive properties," *Journal of Energy Chemistry*, vol. 25, no. 4, pp. 601–608, 2016.
- [29] R. Holze, "Piero Zanello: inorganic electrochemistry: theory, practice and applications," *Journal of Solid State Electrochemistry*, vol. 10, no. 7, pp. 512–513, 2006.
- [30] D. Han, P. Xu, X. Jing et al., "Trisodium citrate assisted synthesis of hierarchical NiO nanospheres with improved supercapacitor performance," *Journal of Power Sources*, vol. 235, no. 4, pp. 45–53, 2013.
- [31] M. Yu, J. Chen, J. Liu et al., "Mesoporous NiCo₂O₄ nanoneedles grown on 3D graphene-nickel foam for supercapacitor and methanol electro-oxidation," *Electrochimica Acta*, vol. 151, pp. 99–108, 2015.
- [32] H. Chen, Y. Ai, F. Liu et al., "Carbon-coated hierarchical Ni-Mn layered double hydroxide nanoarrays on Ni foam for flexible high-capacitance supercapacitors," *Electrochimica Acta*, vol. 213, pp. 55–65, 2016.
- [33] L. Li, P. Gao, S. Gai et al., "Ultra small and highly dispersed Fe₃O₄ nanoparticles anchored on reduced graphene for supercapacitor application," *Electrochimica Acta*, vol. 190, pp. 566–573, 2016.
- [34] H. Xiao, S. Yao, H. Liu, F. Qu, X. Zhang, and X. Wu, "NiO nanosheet assembles for supercapacitor electrode materials," *Progress in Natural Science: Materials International*, vol. 26, no. 3, pp. 271–275, 2016.
- [35] J.-Y. Shieh, S.-Y. Tsai, B.-Y. Li, and H. H. Yu, "High-performance flexible supercapacitor based on porous array electrodes," *Materials Chemistry and Physics*, vol. 195, pp. 114–122, 2017.
- [36] T.-S. Hyun, H.-G. Kim, and I.-D. Kim, "Facile synthesis and electrochemical properties of conducting SrRuO₃-RuO₂ composite nanofibre mats," *Journal of Power Sources*, vol. 195, no. 5, pp. 1522–1528, 2010.
- [37] H. Yang, Z. Yang, X. Wen, and L. Liu, "The in-situ growth of zinc-aluminum layered double hydroxides on graphene and its application as anode active materials for Zn-Ni secondary battery," *Electrochimica Acta*, vol. 252, pp. 507–515, 2017.
- [38] X. Lv, G. Li, Z. Pang et al., "Fabricate BC/Fe₃O₄@PPy 3D nanofiber film as flexible electrode for supercapacitor application," *Journal of Physics and Chemistry of Solids*, vol. 116, pp. 153–160, 2018.
- [39] J. Chen, J. Qiu, B. Wang, H. Feng, K. Ito, and E. Sakai, "Fe₃O₄/biocarbon composites with superior performance in supercapacitors," *Journal of Electroanalytical Chemistry*, vol. 804, pp. 232–239, 2017.
- [40] S. G. Mohamed, S. Y. Attia, and H. H. Hassan, "Spinel-structured FeCo₂O₄ mesoporous nanosheets as efficient electrode for supercapacitor applications," *Microporous and Mesoporous Materials*, vol. 251, pp. 26–33, 2017.
- [41] A. Pendashteh, J. Palma, M. Anderson, and R. Marcella, "Nanostructured porous wires of iron cobaltite: novel positive electrode for high-performance hybrid energy storage devices," *Journal of Materials Chemistry A*, vol. 3, no. 32, pp. 16849–16859, 2015.

- [42] Y. Zhang, S. Yu, G. Lou et al., "Review of macroporous materials as electrochemical supercapacitor electrodes," *Journal of Materials Science*, vol. 52, no. 19, pp. 11201–11228, 2017.
- [43] K. Vijaya Sankar and R. Kalai Selvan, "Improved electrochemical performances of reduced graphene oxide based supercapacitor using redox additive electrolyte," *Carbon*, vol. 90, pp. 260–273, 2015.
- [44] Q. X. Xia, K. San Hui, K. N. Hui et al., "Facile synthesis of manganese carbonate quantum dots/Ni(HCO₃)₂-MnCO₃ composites as advanced cathode materials for high energy density asymmetric supercapacitors," *Journal of Materials Chemistry A*, vol. 3, no. 44, pp. 22102–22117, 2015.



Hindawi
Submit your manuscripts at
www.hindawi.com

